How to cite: *Angew. Chem. Int. Ed.* **2024**, *63*, e202410241
doi.org/10.1002/anie.202410241

Photodynamic Therapy

Nanoscale Metal-Organic Layer Reprograms Cellular Metabolism to Enhance Photodynamic Therapy and Antitumor Immunity

*Gan Lin[+], Langston Tillman[+], Taokun Luo, Xiaomin Jiang, Yingjie Fan, Gang Liu, and Wenbin Lin**

Abstract: Abnormal cancer metabolism causes hypoxic and immunosuppressive tumor microenvironment (TME), which limits the antitumor efficacy of photodynamic therapy (PDT). Herein, we report a photosensitizing nanoscale metal–organic layer (MOL) with anchored 3-bromopyruvate (BrP), BrP@MOL, as a metabolic reprogramming agent to enhance PDT and antitumor immunity. BrP@MOL inhibited mitochondrial respiration and glycolysis to oxygenate tumors and reduce lactate production. This metabolic reprogramming enhanced reactive oxygen species generation during PDT and reshaped the immunosuppressive TME to enhance antitumor immunity. BrP@MOL-mediated PDT inhibited tumor growth by >90% with 40% of mice being tumor-free, rejected tumor re-challenge, and prevented lung metastasis. Further combination with immune checkpoint blockade potently regressed the tumors with >98% tumor inhibition and 80% of mice being tumor-free.

Photodynamic therapy (PDT) generates cytotoxic reactive oxygen species (ROS) to kill tumor cells and activate immune responses.[1] However, ROS generation is impeded by hypoxia in advanced tumors, while PDT-mediated immune responses can be dampened by the immunosuppressive tumor microenvironment (TME).[2] The hypoxic and immunosuppressive features of the TME are predominantly driven by abnormal cellular metabolism.[3] Excessive mitochondrial metabolism leads to overconsumption of oxygen and results in hypoxia.[2a,4] The aberrant glycolysis of cancer cells generates immunosuppressive metabolites, such as lactic acid, to impair T cell function and suppress antitumor immunity.[5] Metabolic reprogramming of cancer cells is an important therapeutic target for cancers.[6]

Nanotechnology offers promising approaches to design nano-photosensitizers for PDT[7] and deliver metabolic agents to reprogram cellular metabolism to enhance PDT.[8] We recently developed two-dimensional (2D) nanoscale metal-organic layers (MOLs) as a new class of nano-photosensitizers.[9] Herein, we report a novel 2D nano-photosensitizer, BrP@MOL (BrP is 3-bromopyruvate, an inhibitor of mitochondrial respiration and glycolysis[10]), for alleviating hypoxic and immunosuppressive TMEs via metabolic reprograming (Figure 1). Although BrP has been previously used as a respiration inhibitor to enhance PDT,[11] we aim to not only enhance PDT via tumor oxygenation but also alleviate the immunosuppressive TME with MOL-loaded BrP. BrP@MOL was synthesized by anchoring BrP on Hf-DBP MOL. BrP@MOL induced tumor oxygenation

[*] Dr. G. Lin,[+] Dr. T. Luo, Dr. X. Jiang, Y. Fan, Prof. W. Lin
Department of Chemistry, The University of Chicago, Chicago, IL 60637 (USA)
Dr. G. Lin,[+] Prof. G. Liu
State Key Laboratory of Molecular Vaccinology and Molecular Diagnostics & Center for Molecular Imaging and Translational Medicine, School of Public Health, Xiamen University, Xiamen 361102, China
L. Tillman[+]
Pritzker School of Molecular Engineering, The University of Chicago, Chicago, IL 60637, USA
Prof. W. Lin
Department of Radiation and Cellular Oncology and Ludwig Center for Metastasis Research, The University of Chicago, Chicago, IL 60637, USA
E-mail: wenbinlin@uchicago.edu
[+] These authors contributed equally to this work.

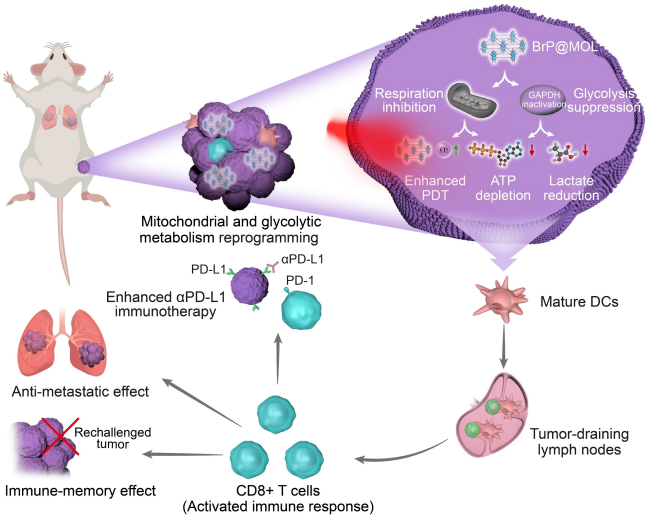

Figure 1. . Schematic illustration of BrP@MOL-mediated mitochondrial and glycolysis metabolic reprogramming for enhanced PDT and antitumor immunity.

and reduced lactate production by suppressing mitochondrial and glycolytic metabolism, leading to enhanced PDT and immune activation. This photo-metabolic therapy significantly improved antitumor effects of PDT, rejected tumor re-challenge, and prevented lung metastasis of breast cancer. Further combination with anti-PD-L1 resulted in tumor regression with 80 % of mice being tumor-free.

Hf-DBP MOL was synthesized via a solvothermal reaction between $HfCl_4$ and 5,15-dip-benzoatoporphyrin (H_2DBP) in *N,N*-dimethylformamide at 80 °C (Figure 2a, Figures S1–3).[9a] Built from Hf_{12} secondary building units (SBUs) and DBP bridging ligands, MOL possesses a 2D structure of **kgd** topology and a formula of $Hf_{12}(\mu_3\text{-}O)_8(\mu_3\text{-}OH)_8(\mu_2\text{-}OH)_6(DBP)_6(\mu_2\text{-}PA)_6$ (PA is propionate). ^{1}H NMR analysis of the digested MOL confirmed a PA to DBP ratio of 1:1 (Figure S3). The coordinating PA was replaced by trifluoroacetic acid (TFA), which was supported ^{1}H and ^{19}F NMR analysis (Figure S4).

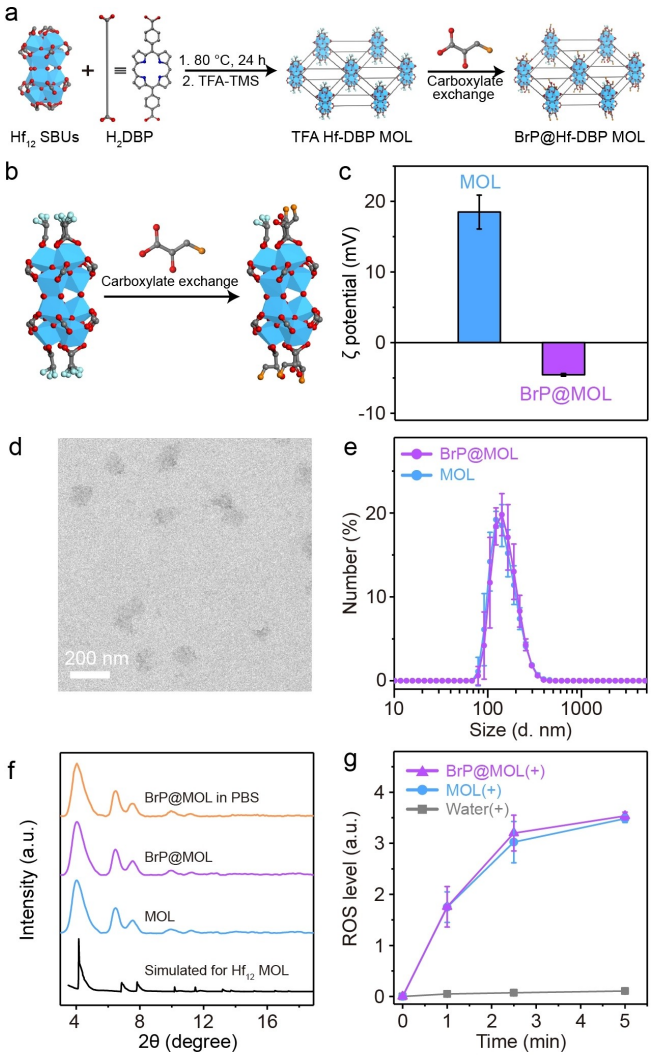

Figure 2. (a) Synthetic scheme of BrP@MOL. (b) Schematic illustration of BrP loading on MOL. (c) Zeta (ζ) potentials of MOL and BrP@MOL ($n=3$). (d) TEM image of BrP@MOL. (e) Number-averaged diameters of MOL and BrP@MOL ($n=3$). (f) PXRD patterns of MOL, BrP@MOL, and the simulated pattern of Hf_{12}-MOL. (g) ROS generation by MOL and BrP@MOL under light irradiation ($n=3$). Data are presented as mean ± SD.

BrP was conjugated to the SBUs by partially substituting TFA via carboxylate exchange to afford BrP@MOL with the formula $Hf_{12}(\mu_3\text{-}O)_8(\mu_3\text{-}OH)_8(\mu_2\text{-}OH)_6(DBP)_6(\mu_2\text{-}BrP)_{4.86}(\mu_2\text{-}TFA)_{1.14}$ (Figure 2b). Conjugation of anionic BrP reversed the zeta potential from +18.5 ± 2.4 mV for MOL to −4.55 ± 0.19 mV for BrP@MOL (Figure 2c). The BrP-to-DBP ratio was determined as 0.81 by ^{1}H NMR (Figure S5). TEM and atomic force microscopy imaging showed that BrP@MOL maintained the nanoplate structure of MOL, with a diameter of ~150 nm (Figures 2d, S6–7). Dynamic light scattering measurements gave number-averaged sizes of 153.7 ± 7.2 and 157.2 ± 9.0 for MOL and BrP@MOL, respectively (Figure 2e). Powder X-ray diffraction (PXRD) studies showed that BrP@MOL retained the crystalline structure of MOL and was stable in phosphate-buffered saline (PBS) buffer (Figure 2f). BrP was slowly released from BrP@MOL upon incubation in 1× PBS and 0.1× PBS, resulting in 74.6 % and 47.9 % BrP release, respectively, in 48 hours (Figure S9).

MOL and BrP@MOL generated similar levels of ROS in test tubes under light irradiation (Figure 2g; 630 nm, 80 mW/cm^2; "+" denotes light irradiation) by 2′,7′–dichlorofluorescein (DCF) assays. However, BrP@MOL(+) generated significantly more intracellular ROS than MOL(+) by confocal laser scanning microscopy (CLSM) imaging (Figure 3a, S10). Flow cytometry analysis revealed that BrP@MOL(+) produced twice intracellular ROS as MOL(+) (Figure S11). As MOL and BrP@MOL showed comparable ROS generation in test tubes and similar cellular uptake (Figure S12), enhanced intracellular ROS generation by BrP@MOL(+) could be attributed to mitochondrial metabolic reprogramming (Figure 4a). As an inhibitor of mitochondrial respiration, BrP can suppress mitochondrial respiratory activities to reduce oxygen consumption and increase intracellular oxygen levels for enhanced PDT.[10b,11] Intracellular O_2 was measured with an oxygen-quenchable dye. BrP and BrP@MOL treatments resulted in a 2-fold reduction in mean fluorescence intensity (MFI) in comparison to MOL and PBS groups (Figure S13).

We next examined the metabolic states of CT26 cells via analyzing the fluorescence intensity and lifetime of flavin adenine dinucleotide (FAD) by fluorescence lifetime imaging. As a crucial cofactor of mitochondrial respiration, cellular FAD level is related to mitochondrial respiratory activity.[12] Additionally, FAD exists in two forms: free FAD with a longer fluorescence lifetime and protein-bound FAD with a shorter fluorescence lifetime. When the intracellular oxygen level is elevated, there is an increased level of FAD in the free form with an increased fluorescence lifetime.[13] BrP@MOL-treated cells exhibited 34.8 % and 32.1 % lower FAD fluorescence intensity than PBS and MOL-treated cells, respectively (Figure 4b, c), indicating the reduced abundance of FAD and impaired mitochondrial respiration.[12a,14] BrP@MOL-treated cells showed 0.484 ns and 0.520 ns longer average FAD fluorescence lifetime (τ_{avg}) than PBS- and MOL-treated cells, respectively (Figure 4d,

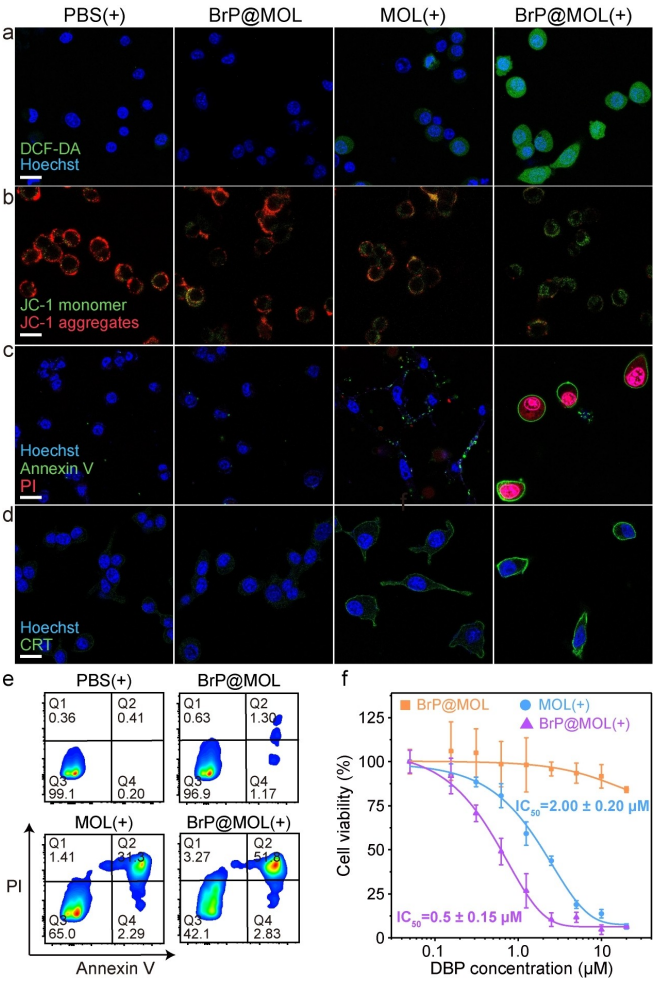

Figure 3. CLSM images showing DCF-DA staining (a), JC-1 staining (b), Annexin-V (green) and PI (red) double staining (c), and CRT surface translocation (green, d) of CT26 cells. Scale bar: 20 μm. (e) Flow cytometric analysis showing Annexin V/PI staining of CT26 cells. (f) CT26 cell viability ($n=3$). Data are presented as mean ± SD.

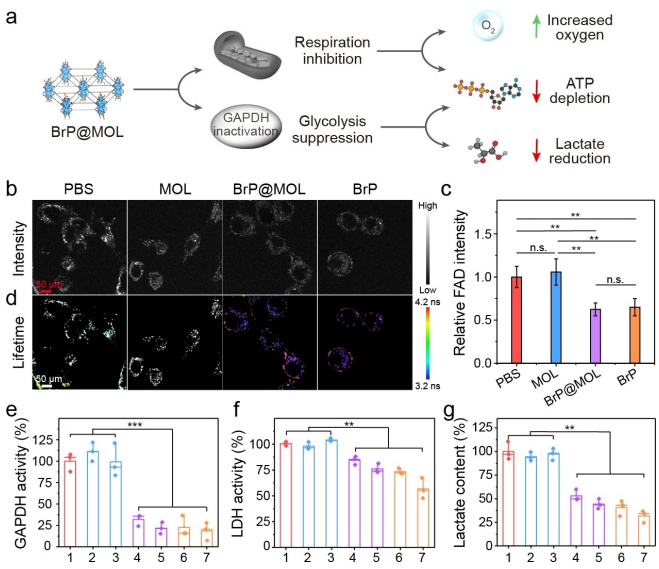

Figure 4. (a) Schematic illustration of mitochondrial and glycolysis metabolic reprogramming by BrP@MOL. (b, c, d) Fluorescence intensity (b, c) and representative pseudocolor mapping of average fluorescence lifetime (d) of FAD in CT26 cells; Scale bar: 50 μm. $n=10$ in c. (e, f, g) GAPDH activity (e), LDH activity (f), and intracellular lactate concentration (g) of CT26 cells. 1: PBS, 2: MOL (24 h), 3: MOL (48 h), 4: BrP@MOL (24 h), 5: BrP@MOL (48 h), 6: BrP (24 h), 7: BrP (48 h). $n=3$ in e, f, g. Data are presented as mean ± SD. **, $p<0.01$; ***, $p<0.001$.

S14). Moreover, BrP@MOL-treated cells showed 2.40- and 2.41-fold higher free- to protein-bound FAD ratio (a_2/a_1 ratio) than PBS- and MOL-treated cells, respectively. The increased τ_{avg} value and higher a_2/a_1 ratio of BrP@MOL-treated cells indicated the presence of more free FAD due to an increased intracellular oxygen level. These findings support the reprogramming of mitochondrial metabolism by BrP@MOL to reduce mitochondrial respiratory activities.

BrP@MOL-mediated metabolic regulation was assessed by glycolysis-related markers, glyceraldehyde 3-phosphate dehydrogenase (GAPDH) and lactate dehydrogenase (LDH) (Figure 4e, f, g, S15). BrP@MOL-treated CT26 cells showed 66.9 % and 74.9 % lower GAPDH activity than PBS control at 24 h and 48 h post treatment. Additionally, BrP@MOL treatment reduced LDH activity to 85.4 % and 78.0 % of PBS control at 24 h and 48 h. Consequently, BrP@MOL reduced lactate concentration to 53.0 % and 44.2 % of PBS control at 24 h and 48 h, respectively, and ATP production to 74.0 % and 48.5 % of PBS control at 24 h and 48 h, respectively (Figure S16). In contrast, MOL showed negligible inhibitory effects on glycolysis-related markers. These findings support glycolysis inhibition by BrP@MOL to reduce lactate concentration.

BrP@MOL(+) increased depolarization of mitochondrial membrane potential with an increase in JC-1 monomer fluorescence (Figure 3b, S17). BrP@MOL(+) also stimulated stronger apoptosis and immunogenic cell death (ICD) than MOL(+) and BrP@MOL (Figures 3c, d, e, S18–22). Annexin V/propidium iodide (PI) staining showed that BrP@MOL(+) induced 21.0 % and 52.2 % more apoptotic cell death than MOL(+) and BrP@MOL, respectively, at a DBP concentration of 2.5 μM. Negligible apoptotic cell death was observed in dark controls and PBS(+). BrP@MOL(+)-treated cells showed 2.6-, 2.6-, and 1.0-fold higher calreticulin (CRT) translocation, 5.63-, 3.07- and 2.05-fold higher ATP secretion, and 12.6-, 135-, and 2.32-fold higher high mobility group box 1 (HMGB1) release than PBS, BrP@MOL, and MOL(+) groups, respectively.

BrP@MOL(+) induced significantly higher cytotoxicity with half maximal inhibitory concentration (IC_{50}) values of 0.50 and 1.12 μM for CT26 and 4T1 cells, respectively (Figure 3f, S23; Tables S1 and S2). These IC_{50} values were 4.0- and 2.7-fold lower than those of MOL(+) for CT26 and 4T1 cells, respectively. In comparison, BrP@MOL exhibited only slight cytotoxicity at high concentrations, while MOL showed negligible cytotoxicity on CT26 and 4T1 cells (Figure S25). The synergy between PDT and metabolic reprogramming was supported by low combination indices of BrP@MOL(+) (Tables S3 and S4).[15]

The antitumor efficacy of BrP@MOL(+) was determined in a subcutaneous CT26 colorectal adenocarcinoma mouse model and an orthotopic 4T1 murine triple-negative breast cancer model. Tumor-bearing mice were intratumorally injected with BrP@MOL, MOL, or PBS at a DBP dose of 0.2 μmol (or 0.162 μmol BrP) at day 7 and 9 post tumor inoculation and irradiated (630 nm, 80 mW/cm^2, 15 mins) 8 hours later. Tumor sizes and body weights were recorded daily. The mice were euthanized on day 19 (CT26) or day 23 (4T1) when the PBS groups reached the endpoints. The tumors were excised, weighed, and photographed. BrP@MOL(+) treatment regressed the tumors with tumor growth inhibition (TGI) values of 93.6 % and 91.4 % for CT26 and 4T1 tumors, respectively (Figure 5a, f). In contrast, BrP@MOL and MOL(+) displayed moderate TGI values of 47.6 % and 65.0 %, respectively, for CT26 model and 41.9 % and 56.0 %, respectively, for 4T1 model. BrP showed a slightly lower TGI than BrP@MOL, while MOL had no antitumor effect. BrP@MOL(+) treatment eradicated tumors in 40 % and 20 % of CT26- and 4T1 tumor-bearing mice, respectively, while other treatment groups had no tumor-free mice. The strong antitumor effects of BrP@MOL(+) were supported by the tumor photos and weights at the endpoints (Figure 5b, c, S26).

Hematoxylin and eosin (H&E) staining and Terminal deoxynucleotidyl transferase dUTP nick end labeling (TUNEL) assays showed that BrP@MOL(+)-treated tumors had the lowest cancer cell densities and the highest levels of DNA fragmentations (Figure 5d, S27). All treatments had negligible side effects as indicated by steady bodyweights and lack of abnormality in the histology of major organs (Figures S28–30).

We also investigated metabolic reprogramming and immune responses of CT26 tumors in vivo. BrP@MOL-treated tumors showed 60.0 % and 33.3 % reduction of GAPDH activity and lactate concentration, respectively, when compared to PBS control (Figure 6a, b). BrP@MOL-treated CT26 tumors also displayed a decreased level of carbonic anhydrase 9 (CA9) and hypoxia-inducible factor 1-alpha, both biomarkers of hypoxia (Figure 6c, S31).

We next examined dendritic cell (DC) population and maturation after different treatments. The tumor-draining lymph nodes (TDLNs) of CT26 tumor-bearing mice were collected and analyzed by flow cytometry, the population was assessed by the expression of MHC II/CD11c (DCs

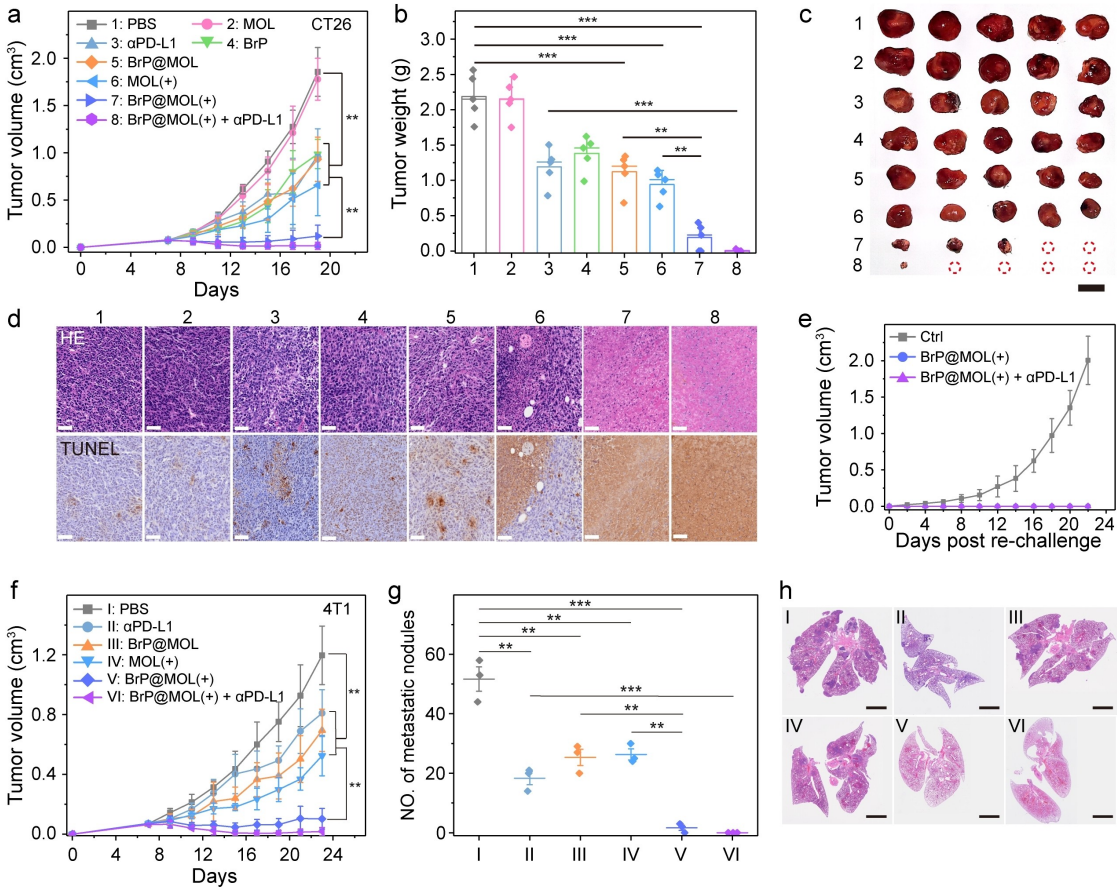

Figure 5. Growth curves (a), and tumor weights (b) and photos (c) of subcutaneous CT26 tumors ($n=5$). Scale bar = 1.5 cm in c. (d) H&E and TUNEL staining of CT26 tumors. Scale bars = 100 μm. (e) Growth curves of rechallenged CT26 tumors ($n=4$). (f) Growth curves of orthotopic 4T1 tumors ($n=5$). Number of metastatic nodules (g) and H&E staining (h) of the lungs excised from 4T1 tumor-bearing mice. n = 3 in g. Scale bars = 2 mm in h. Data are presented as mean ± SD. **, $p<0.01$; ***, $p<0.001$.

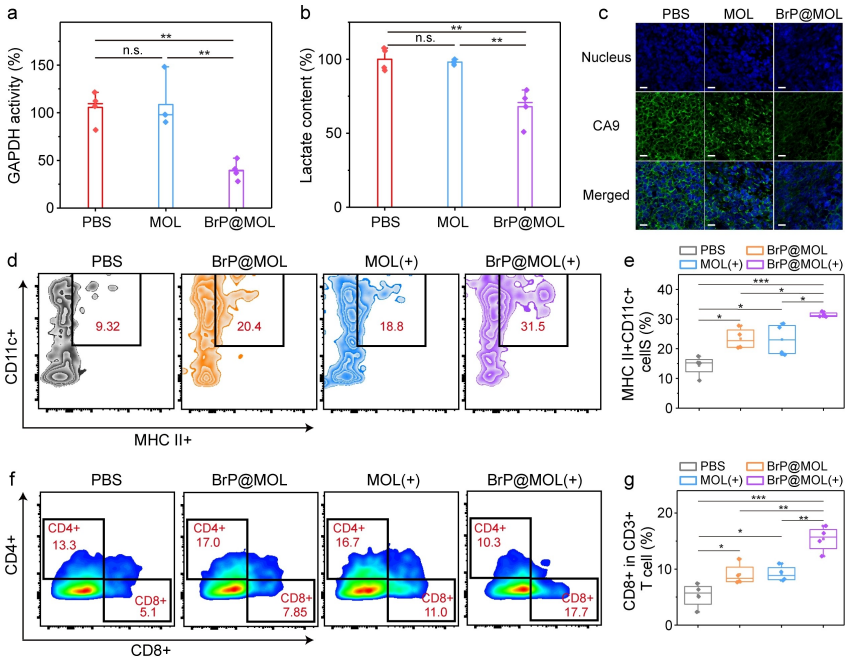

Figure 6. GAPDH activity (a) and lactate concentration (b) of excised CT26 tumors ($n=4$). (c) Immunofluorescence staining of CA9 (green) in CT26 tumors. Flow cytometry plots (d) and quantification (e) of DCs (MHC II+CD11c+) in the TDLNs from CT26 tumor-bearing mice. Flow cytometry plots (f) and quantification (g) of CD8+T cells in CT26 tumors. $n=4$ in e and g. Data are presented as mean±SD. *, $p<0.05$; **, $p<0.01$; ***, $p<0.001$.

biomarker), and the maturation was assessed by CD80, a biomarker of mature DCs (mDCs). BrP@MOL(+)-treated mice had 32 % DCs in the TDLNs, compared to 23.1 %, 23.4 % and 14.3 % in MOL(+), BrP@MOL(−) and PBS group, indicating the remarkable enhancement in DC homing capability into TDLNs following BrP@MOL(+) treatment (Figure 6d, e). Additionally, BrP@MOL(−)- and MOL(+)-treated mice had 56.2 % and 46.9 % mDCs in the TDLNs, compared to 18.8 % in PBS group (Figure S33), suggesting DC activation by both tumor metabolic reprogramming and PDT treatment.[16] BrP@MOL(−)- and MOL-(+)-treated tumors showed 1.71- and 1.73-fold higher CD8+ T cells than PBS-treated tumors. BrP@MOL(+)-treated tumors showed 2.89-fold higher CD8+ T cells than that of PBS-treated tumors (Figure 6f, g).

As BrP@MOL(+) treatment upregulated PD-L1 expression (Figure S35), we combined BrP@MOL(+) with anti-PD-L1 antibody (αPD-L1, 100 μg/mouse) to evaluate their synergy. BrP@MOL(+) plus αPD-L1 further enhanced the antitumor efficacy to regress CT26 and 4T1 tumors with TGI values of 99.1 % and 98.5 %, respectively, and with 80 % and 60 % of mice being tumor-free, respectively. The immune-memory of the antitumor effects was assessed by re-challenging the tumor-free mice after BrP@MOL(+) or BrP@MOL(+) plus αPD-L1 treatment 11 days after the PBS end point. The tumor-free mice completely rejected tumor challenge (Figure 5e), while naïve mice developed tumors aggressively. We also examined the antimetastatic effects of BrP@MOL(+) on the orthotopic 4T1 model, which is known to develop lung metastasis. PBS, BrP@MOL, MOL-(+), and BrP@MOL(+) groups showed 51.6±7.1, 25.3±4.7, 26.3±4.2, and 1.66±1.5 pulmonary metastatic nodules, respectively (Figure 5g, h). Finally, RNA-seq results showed that BrP@MOL(+) altered cancer metabolism, induced strong tumor apoptosis, and enhanced immune cell infiltration and immune response (Figure S37).

In summary, we developed a BrP-loaded 2D nano-photosensitizer for simultaneous PDT enhancement and immune activation via metabolic reprogramming. BrP@MOL reshaped the hypoxic and immunosuppressive TME via altering mitochondrial and glycolytic metabolism. BrP@MOL-mediated PDT inhibited tumor growth by >90 % with 40 % of mice being tumor free, rejected tumor re-challenge, and prevented lung metastasis. Further combination with αPD-L1 potently regressed the tumors with >98 % tumor inhibition and with 80 % of mice being tumor-free. This work uncovers a novel nanomaterial-based photo-metabolic strategy to enhance PDT efficacy and antitumor immunity.

Supporting Information

The authors have cited additional references within the Supporting Information.

Acknowledgements

We thank Jianming Mao, Dr. Qingyun Guo, and Zitong Wang for help with MOL synthesis and characterization. We thank Prof. Vytautas Bindokas, Dr. Christine Labno,

and Shirley Bond for help with Fluorescence lifetime imaging, confocal imaging, and whole-slide scanning. We acknowledge funding from the National Cancer Institute (1R01CA253655). G.L. was supported by a postdoctoral fellowship from Xiamen University. This work used the shared facilities at the University of Chicago Materials Research Science and Engineering Center, supported by the National Science Foundation under award number DMR-2011854.

Conflict of Interest

The authors declare no conflict of interest.

Data Availability Statement

The data that support the findings of this study are available from the corresponding author upon reasonable request.

Keywords: metal-organic layers · cancer metabolism · photodynamic therapy · two-dimensional materials · antitumor immunity

[1] a) M. A. Rajora, J. W. H. Lou, G. Zheng, *Chem. Soc. Rev.* **2017**, *46*, 6433–6469; b) B. Chen, Y. Yan, Y. Yang, G. Cao, X. Wang, Y. Wang, F. Wan, Q. Yin, Z. Wang, Y. Li, L. Wang, B. Xu, F. You, Q. Zhang, Y. Wang, *Nat. Nanotechnol.* **2022**, *17*, 788–798; c) X. Li, J. F. Lovell, J. Yoon, X. Chen, *Nat. Rev. Clin. Oncol.* **2020**, *17*, 657–674; d) J. Chen, Y. Zhu, C. Wu, J. Shi, *Chem. Soc. Rev.* **2023**, *52*, 973–1000.

[2] a) J. Nam, S. Son, K. S. Park, W. Zou, L. D. Shea, J. J. Moon, *Nat. Rev. Mater.* **2019**, *4*, 398–414; b) Y. Lu, W. Sun, J. Du, J. Fan, X. Peng, *JACS Au* **2023**, *3*, 682–699; c) D. Wang, H. Wu, W. Q. Lim, S. Z. F. Phua, P. Xu, Q. Chen, Z. Guo, Y. Zhao, *Adv. Mater.* **2019**, *31*, 1901893; d) J. A. Joyce, D. T. Fearon, *Science* **2015**, *348*, 74–80; e) J. Li, K. T. Byrne, F. Yan, T. Yamazoe, Z. Chen, T. Baslan, L. P. Richman, J. H. Lin, Y. H. Sun, A. J. Rech, D. Balli, C. A. Hay, Y. Sela, A. J. Merrell, S. M. Liudahl, N. Gordon, R. J. Norgard, S. Yuan, S. Yu, T. Chao, S. Ye, T. S. K. Eisinger-Mathason, R. B. Faryabi, J. W. Tobias, S. W. Lowe, L. M. Coussens, E. J. Wherry, R. H. Vonderheide, B. Z. Stanger, *Immunity* **2018**, *49*, 178–193.e177.

[3] a) D. Hanahan, *Cancer Dis.* **2022**, *12*, 31–46; b) A. van Weverwijk, K. E. de Visser, *Nat. Rev. Cancer* **2023**, *23*, 193–215.

[4] a) M. Li, Y. Xu, X. Peng, J. S. Kim, *Acc. Chem. Res.* **2022**, *55*, 3253–3264; b) G. Lin, J. Zhou, H. Cheng, G. Liu, *Small* **2023**, *n/a*, 2207973.

[5] a) M. J. Watson, P. D. A. Vignali, S. J. Mullett, A. E. Overacre-Delgoffe, R. M. Peralta, S. Grebinoski, A. V. Menk, N. L. Rittenhouse, K. DePeaux, R. D. Whetstone, D. A. A. Vignali, T. W. Hand, A. C. Poholek, B. M. Morrison, J. D. Rothstein, S. G. Wendell, G. M. Delgoffe, *Nature* **2021**, *591*, 645–651; b) S. Kumagai, S. Koyama, K. Itahashi, T. Tanegashima, Y.-t. Lin, Y. Togashi, T. Kamada, T. Irie, G. Okumura, H. Kono, D. Ito, R. Fujii, S. Watanabe, A. Sai, S. Fukuoka, E. Sugiyama, G. Watanabe, T. Owari, H. Nishinakamura, D. Sugiyama, Y. Maeda, A. Kawazoe, H. Yukami, K. Chida, Y. Ohara, T. Yoshida, Y. Shinno, Y. Takeyasu, M. Shirasawa, K. Nakama, K. Aokage, J. Suzuki, G. Ishii, T. Kuwata, N. Sakamoto, M. Kawazu, T. Ueno, T. Mori, N. Yamazaki, M. Tsuboi, Y. Yatabe, T. Kinoshita, T. Doi, K. Shitara, H. Mano, H. Nishikawa, *Cancer Cell* **2022**, *40*, 201–218.e209; c) K. DePeaux, G. M. Delgoffe, *Nat. Rev. Immunol.* **2021**, *21*, 785–797.

[6] a) K. Vasan, M. Werner, N. S. Chandel, *Cell Metab.* **2020**, *32*, 341–352; b) Y. Tan, J. Li, G. Zhao, K.-C. Huang, H. Cardenas, Y. Wang, D. Matei, J.-X. Cheng, *Nat. Commun.* **2022**, *13*, 4554; c) G. Lu, X. Wang, F. Li, S. Wang, J. Zhao, J. Wang, J. Liu, C. Lyu, P. Ye, H. Tan, W. Li, G. Ma, W. Wei, *Nat. Commun.* **2022**, *13*, 4214.

[7] a) M. Zhao, H. Zhuang, B. Li, M. Chen, X. Chen, *Adv. Mater.* **2023**, *n/a*, 2209944; b) F. Fang, S. Wang, Y. Song, M. Sun, W.-C. Chen, D. Zhao, J. Zhang, *Nat. Commun.* **2023**, *14*, 1660; c) J. Park, Q. Jiang, D. Feng, L. Mao, H.-C. Zhou, *J. Am. Chem. Soc.* **2016**, *138*, 3518–3525.

[8] a) X. Jiang, M. Lee, J. Xia, T. Luo, J. Liu, M. Rodriguez, W. Lin, *ACS Nano* **2022**; b) M. Li, Y. Shao, J. H. Kim, Z. Pu, X. Zhao, H. Huang, T. Xiong, Y. Kang, G. Li, K. Shao, J. Fan, J. W. Foley, J. S. Kim, X. Peng, *J. Am. Chem. Soc.* **2020**, *142*, 5380–5388.

[9] a) T. Luo, Y. Fan, J. Mao, E. Yuan, E. You, Z. Xu, W. Lin, *J. Am. Chem. Soc.* **2022**, *144*, 5241–5246; b) G. Lin, G. T. Nash, T. Luo, I. Ghosh, S. Sohoni, A. J. Christofferson, G. Liu, G. S. Engel, W. Lin, *Adv. Mater.* **2023**, *n/a*, 2212069.

[10] a) Z. E. Stine, Z. T. Schug, J. M. Salvino, C. V. Dang, *Nat. Rev. Drug Discovery* **2022**, *21*, 141–162; b) M. C. Shoshan, *J. Bioenerg. Biomembr.* **2012**, *44*, 7–15.

[11] a) Y. Deng, P. Song, X. Chen, Y. Huang, L. Hong, Q. Jin, J. Ji, *ACS Nano* **2020**, *14*, 9711–9727; b) L. Zuo, W. Nie, S. Yu, W. Zhuang, G. Wu, H. Liu, L. Huang, D. Shi, X. Sui, Y. Li, H.-Y. X, *Angew. Chem.* **2021**, *60*, 25365–25371; c) Z. Wang, H. Li, W. She, X. Zhang, Y. Liu, Y. Liu, P Jiang, *Anal. Chem.* **2023**, *95*, 1710–1720.

[12] a) F. J. Gerich, S. Hepp, I. Probst, M. Müller, *J. Neurophysiol.* **2006**, *96*, 492–504; b) K. M. Holmström, L. Baird, Y. Zhang, I. Hargreaves, A. Chalasani, J. M. Land, L. Stanyer, M. Yamamoto, A. T. Dinkova-Kostova, A. Y. Abramov, *Biology Open* **2013**, *2*, 761–770.

[13] R. Penjweini, B. Roarke, G. Alspaugh, A. Gevorgyan, A. Andreoni, A. Pasut, D. L. Sackett, J. R. Knutson, *Redox Biology* **2020**, *34*, 101549.

[14] M. S. Islam, M. Honma, T. Nakabayashi, M. Kinjo, N. Ohta, in *International Journal of Molecular Sciences, Vol. 14*, **2013**, pp. 1952–1963.

[15] G. Lin, Y. Zhang, C. Zhu, C. Chu, Y. Shi, X. Pang, E. Ren, Y. Wu, P. Mi, H. Xia, X. Chen, G. Liu, *Biomaterials* **2018**, *176*, 60–70.

[16] J. Park, L. Wang, P.-C. Ho, *Oncogenesis* **2022**, *11*, 62.

Manuscript received: May 30, 2024
Accepted manuscript online: June 25, 2024
Version of record online: August 12, 2024